

Article

Open Access



# Rational design of nitrogen-doping $Ti_3C_2T_x$ microspheres with enhanced polysulfide catalytic activity for lithium-sulfur batteries

Lucheng Cai<sup>#</sup>, Hangjun Ying<sup>#</sup> , Chaowei He, Hui Tan, Pengfei Huang, Qizhen Han, Wei-Qiang Han<sup>\*</sup>

School of Materials Science and Engineering, Zhejiang University, Hangzhou 310058, Zhejiang, China.

<sup>#</sup>Authors contributed equally.

\*Correspondence to: Prof./Dr. Wei-Qiang Han, School of Materials Science and Engineering, Zhejiang University, 866 Yuhangtang Rd., Hangzhou 310058, Zhejiang, China. E-mail: hanwq@zju.edu.cn

**How to cite this article:** Cai L, Ying H, He C, Tan H, Huang P, Han Q, Han WQ. Rational design of nitrogen-doping  $Ti_3C_2T_x$  microspheres with enhanced polysulfide catalytic activity for lithium-sulfur batteries. *Energy Mater* 2024;4:400051. <https://doi.org/10.20517/energymater.2023.104>

**Received:** 13 Dec 2023 **First Decision:** 21 Mar 2024 **Revised:** 4 Apr 2024 **Accepted:** 6 May 2024 **Published:** 23 May 2024

**Academic Editors:** Jiazhao Wang, Jinkui Feng **Copy Editor:** Fangyuan Liu **Production Editor:** Fangyuan Liu

## Abstract

The primary challenges that impede the practical applications of lithium-sulfur batteries are the significant shuttle effect of polysulfides, huge volume expansion, and slow redox kinetics. In this work, three-dimensional nitrogen doping  $Ti_3C_2T_x$  MXenes (3D N- $Ti_3C_2T_x$ ) were successfully synthesized by spray drying and subsequent annealing, and hydrochloric acid-treated melamine effectively reduces the oxidation of MXenes in these processes. The formation of a unique nanoflower-shaped microsphere endows 3D N- $Ti_3C_2T_x$  with a significant specific surface area and pore volume. The combination of nitrogen doping and the large specific surface area increased adsorption capacity and catalytic conversion ability for polysulfide intermediates. Consequently, the obtained 3D N- $Ti_3C_2T_x/S$  cathode exhibited high-capacity retention (578.5 mAh g<sup>-1</sup> after 500 cycles at 0.5 C and 462.5 mAh g<sup>-1</sup> after 1,000 cycles at 1 C), superior rate performance (651.2 mAh g<sup>-1</sup> at 3 C), and excellent long-term cycling performance (capacity fading rate of 0.076% per cycle at 0.5 C and 0.046% per cycle at 1 C). This work expands the potential applications of MXenes for lithium-sulfur batteries.

**Keywords:** MXenes, spray drying, nitrogen doping, catalytic conversion, lithium-sulfur batteries



© The Author(s) 2024. **Open Access** This article is licensed under a Creative Commons Attribution 4.0 International License (<https://creativecommons.org/licenses/by/4.0/>), which permits unrestricted use, sharing, adaptation, distribution and reproduction in any medium or format, for any purpose, even commercially, as long as you give appropriate credit to the original author(s) and the source, provide a link to the Creative Commons license, and indicate if changes were made.



## INTRODUCTION

With the rapid progress in energy storage technology, the demand for higher energy density is increasing. Lithium-sulfur (Li-S) batteries have shown tremendous potential because of their high theoretical energy density (2,600 Wh kg<sup>-1</sup>) and theoretical specific capacity (1,675 mAh g<sup>-1</sup>)<sup>[1-3]</sup>. However, their practical applications still face several challenges<sup>[4-6]</sup>, including the poor electronic conductivity of sulfur and the discharge product lithium sulfide (Li<sub>2</sub>S), volume expansion during discharge, sluggish redox reaction kinetics, and the notorious shuttle-effects (polysulfide intermediates (LiPSs) dissolved in electrolyte and reacted with lithium anodes). These issues lead to low discharge capacity and rapid deterioration in performance<sup>[7,8]</sup>.

Advanced cathode host has been developed to solve the aforementioned issues, including carbon and its derivative<sup>[9-11]</sup>, metal (e.g., high-entropy alloy)<sup>[12,13]</sup>, some conducting compounds or polymers<sup>[14,15]</sup>, and so on. Among them, MXenes have received considerable interest. As first proposed by Naguib *et al.* in 2011, they are expressed as M<sub>n+1</sub>X<sub>n</sub>T<sub>x</sub> (n = 1-3), where M represents transition metal; X stands for C or/and N elements; T<sub>x</sub> is the symbol of functional groups on the surface of MXenes<sup>[16]</sup>. It is impressive that MXenes have the following advantages for Li-S batteries compared to traditional carbon materials: (1) inherent metal conductivity<sup>[17,18]</sup>; (2) two-dimensional surface with high activity<sup>[19,20]</sup>; (3) large binding energy with LiPSs based on Lewis's interaction to inhibit shuttle effect<sup>[21,22]</sup>; and (4) effective catalytic effect on the conversion of LiPSs achieved by abundant surface terminations<sup>[23,24]</sup>. It is these advantages that make MXenes also have excellent performance in other metal-sulfur batteries<sup>[25-27]</sup>.

Zhao *et al.* selectively extracted Ti from the Ti<sub>2</sub>SC MAX phase to form carbon/sulfur nanolaminates, suggesting that MXene material is a promising positive carrier for Li-S batteries<sup>[28]</sup>. Liang *et al.* reported the Ti<sub>2</sub>C(OH)<sub>x</sub>/S cathode application, showing that lithium polysulfides have a strong interaction with the "acidic" Ti site and hydroxyl surface groups<sup>[29]</sup>. The electrochemical properties of MXenes can be further improved by stripping multi-layer MXenes into nanosheets with fewer layers<sup>[30,31]</sup>. However, severe agglomeration of MXene nanosheets happened through van der Waals forces and hydrogen bond interactions after stripping, limiting the accessibility of ions and preventing full utilization of functional surface terminations<sup>[32]</sup>. Doping of heterogeneous atoms, such as nitrogen atoms, can enlarge the interlayer spacing and prevent the agglomeration of MXene nanosheets<sup>[33,34]</sup>. For example, in 2017, Wen *et al.* obtained nitrogen-doped MXenes by heat treatment under an ammonia atmosphere<sup>[35]</sup>, effectively expanding the *c*-lattice parameter of MXene sheets. In addition, introducing nitrogen doping into electrodes can effectively improve the adsorption capacity of LiPSs<sup>[36-38]</sup> and confer electrocatalytic activity on MXenes to accelerate the conversion of LiPSs<sup>[38]</sup>. Song *et al.* prepared porous nitrogen-doped Ti<sub>3</sub>C<sub>2</sub> MXenes (P-NTC) using melamine-formaldehyde (MF) nanospheres as hard templates<sup>[39]</sup>. The negatively charged MXene nanosheets on the positively charged MF sphere surface through electrostatic self-assembly and the prepared P-NTC show an interconnect network with different pores, which greatly alleviate the agglomeration of the MXene nanosheets. Due to the synergistic effect of large specific surface area and nitrogen doping, P-NTC showed more effective adsorption and catalytic conversion ability for Li<sub>2</sub>S<sub>4</sub> solution than MXenes (TC) without nitrogen doping.

Herein, three-dimensional nitrogen-doped porous MXene microspheres (3D N-Ti<sub>3</sub>C<sub>2</sub>T<sub>x</sub>) were synthesized by spray drying and subsequent annealing as the host for sulfur. Firstly, a few layers of negatively charged MXene solution were mixed evenly with positively charged hydrochloric acid (HCl)-treated melamine, and the powder was collected by spray drying. Through sequential annealing, 3D N-Ti<sub>3</sub>C<sub>2</sub>T<sub>x</sub> was obtained. The MXene nanosheets formed three-dimensional spherical nanoflower structure, effectively preventing the agglomeration of MXene nanosheets. During the heat treatment, the self-supported melamine decomposes,

effectively increasing the surface area. Therefore, the synthesized 3D N-Ti<sub>3</sub>C<sub>2</sub>T<sub>x</sub> shows a large surface area, which enables the sulfur to be uniformly impregnated into the MXenes layer. Meanwhile, melamine acts as a nitrogen source to introduce nitrogen doping. Remarkably, due to the synergistic effect of large surface area and nitrogen doping, the 3D N-Ti<sub>3</sub>C<sub>2</sub>T<sub>x</sub>/S cathode exhibits excellent electrochemical properties.

## EXPERIMENTAL

### Synthesis of multiple-layer MXene nanosheets

The accordion multiple-layer MXenes were obtained by hydrofluoric acid (HF) etching. The addition of 2 g Ti<sub>3</sub>AlC<sub>2</sub> (MAX phase) to 200 mL HF solution (40%) was conducted multiple times. Stir the above solution continuously at 35 °C for more than four days to remove the Al layer thoroughly. The powder was collected by centrifugation and washed with deionized (DI) water several times. After that, the multiple-layer Ti<sub>3</sub>C<sub>2</sub>T<sub>x</sub> (MXenes) were obtained by drying the above powder at 70 °C under vacuum for 12 h.

### Synthesis of few-layer MXene nanosheets

Then, 2 g Ti<sub>3</sub>C<sub>2</sub>T<sub>x</sub> was added into 40 mL aqueous solution of tetramethylammonium hydroxide (TMAOH, 25 wt%) and stirred at 35 °C for 24 h. The samples were washed with DI water more than two times to remove TMAOH. Few-layer MXene suspension was obtained by sonicating for 1 h and subsequent centrifugation (3,500 r/min for 10 min). Repeat this step for several times.

### Synthesis of positively charged HCl-treated melamine

Melamine exhibits low solubility in aqueous solutions. Adding HCl is an effective way to enhance its water solubility. We introduced 10 g of melamine into 150 mL of anhydrous ethanol and vigorously agitated the mixture for 4 h. Then, 10 mL HCl solution (37 wt%) was added and further stirred for 2 h. The melamine solution underwent centrifugation, followed by thrice washing with ethanol. Subsequently, the product was subjected to vacuum drying at 60 °C for 12 h. This culminated in the attainment of melamine that had undergone HCl treatment, rendering it soluble in water.

### Synthesis of 3D N-Ti<sub>3</sub>C<sub>2</sub>T<sub>x</sub>

First, 3.2 g HCl-treated melamine was poured into 200 mL of the aforementioned few-layered Ti<sub>3</sub>C<sub>2</sub>T<sub>x</sub> MXenes nanosheet solution and agitated for 24 h at room temperature. It is estimated that the mass ratio between the few-layered Ti<sub>3</sub>C<sub>2</sub>T<sub>x</sub> nanosheets and the HCl-treated melamine is 1:16. Subsequently, the powder was obtained through spray drying and positioned within a tubular furnace enriched with an inert atmosphere (Anhui BEQ BTF. 1,200 °C). Gradually raise the temperature at a rate of 5 °C per minute to 700 °C and then maintain it for 2 h. Finally, the three-dimensional nitrogen-doped porous Ti<sub>3</sub>C<sub>2</sub>T<sub>x</sub> MXene microspheres (noted as 3D N-Ti<sub>3</sub>C<sub>2</sub>T<sub>x</sub>) can be collected after the furnace cools to ambient temperature.

Similarly, 3D Ti<sub>3</sub>C<sub>2</sub>T<sub>x</sub> can be obtained, but the MXene solution was not mixed with HCl-treated melamine before spray drying.

### Preparation of the 3D N-Ti<sub>3</sub>C<sub>2</sub>T<sub>x</sub>/S cathode

The sulfur composite was prepared by traditional molten diffusion strategy: the prepared 3D N-Ti<sub>3</sub>C<sub>2</sub>T<sub>x</sub> (or 3D Ti<sub>3</sub>C<sub>2</sub>T<sub>x</sub>) and sulfur powder in a mass ratio of 3:7 were placed in an agate mortar for thorough grinding. Then, the mixture was heated at 155 °C for 18 h. After cooling to room temperature, 3D N-Ti<sub>3</sub>C<sub>2</sub>T<sub>x</sub>/S (or 3D Ti<sub>3</sub>C<sub>2</sub>T<sub>x</sub>/S) can be collected. The cathode was homogeneously blended with 3D N-Ti<sub>3</sub>C<sub>2</sub>T<sub>x</sub>/S (or 3D Ti<sub>3</sub>C<sub>2</sub>T<sub>x</sub>/S), Super P (SP), and polyvinylidene fluoride (PVDF) in N-Methyl-2-pyrrolidone (NMP) and coated on the carbon-coated aluminum foil. Ultimately, we dried it in vacuum at 60 °C for 12 h.

### Physical characterizations

The X-ray diffraction (XRD) patterns were captured by a Rigaku MiniFlex 600 X-ray diffractometer utilizing a Cu K $\alpha$  source within the range of  $2\theta = 2\text{--}80^\circ$ . The field-emission scanning electron microscopy (FESEM, Hitachi, SU-8010), transmission electron microscopy (TEM, FEI Ltd, Tecnai F20), selected area electron diffraction (SAED), and high-resolution TEM (HRTEM) were employed to study the morphology, internal microstructure, and elemental mapping of the samples. The N<sub>2</sub> adsorption/desorption isotherms were acquired through Micromeritics ASAP 2020 Plus HD88. The X-ray photoelectron spectroscopy (XPS) analysis was determined by Thermo Scientific K-Alpha to scrutinize the surface chemistry of the products. The thermogravimetric analysis (TGA) was conducted employing a Pyris diamond analyzer under an air atmosphere with a heating rate of 5 °C/min from 30 to 800 °C. Ultraviolet-visible (UV-vis) spectra were recorded using a Shimadzu UV-3150 UV-vis spectrometer.

### Electrochemical measurements

We employed 3D N-Ti<sub>3</sub>C<sub>2</sub>T<sub>x</sub>/S (or 3D Ti<sub>3</sub>C<sub>2</sub>T<sub>x</sub>/S) as cathodes, with Li foil and Celgard 2500 as the anode and separator, respectively. The batteries were assembled in an Ar-filled glovebox, ensuring minimal exposure to O<sub>2</sub> and H<sub>2</sub>O (both < 0.01 ppm). Additionally, 1 M lithium bis(trifluoromethanesulfonyl)imide (LiTFSI) in 1,3-dioxolane/1,2-dimethoxyethane (DOL/DME, 1:1 by volume) with 1 wt% LiNO<sub>3</sub> was used as electrolyte. To evaluate the electrochemical performance, cyclic voltammetry (CV) measurements were conducted within a potential window of 1.8–2.8 V (vs. Li/Li<sup>+</sup>). Furthermore, electrochemical impedance spectroscopy (EIS) in the frequency range of 0.1 to 1,000 kHz was employed. The galvanostatic charge-discharge (GCD) curves were assessed using the LAND CT3001A system, with the voltage range set as 1.8–2.8 V (vs. Li/Li<sup>+</sup>).

## RESULTS AND DISCUSSION

[Figure 1](#) depicts the synthesizing process of 3D N-Ti<sub>3</sub>C<sub>2</sub>T<sub>x</sub>/S. The Al layer in Ti<sub>3</sub>AlC<sub>2</sub> (MAX phase) was etched by HF to acquire accordion-like multi-layer Ti<sub>3</sub>C<sub>2</sub>T<sub>x</sub> MXene nanosheets. Subsequently, few-layered MXenes can be synthesized by solution-phase flocculation strategy, according to our previous reports<sup>[40]</sup>. The amino group (-NH<sub>2</sub>) in melamine could capture protons (H<sup>+</sup>) from HCl solution, thus forming positively charged melamine through protonation, which can be easily dissolved in DI water<sup>[41]</sup>. Obviously, HCl-melamine can be fully dissolved in DI water [[Supplementary Figure 1](#)].

The aforementioned HCl-treated melamine was mixed with the few-layered Ti<sub>3</sub>C<sub>2</sub>T<sub>x</sub> solution and stirred together. MXene nanosheets possess negative charges due to the presence of surface functional terminations (e.g., -O, -OH, and -F), allowing for the attachment of positively charged melamine onto the surface of Ti<sub>3</sub>C<sub>2</sub>T<sub>x</sub> MXene nanosheets through electrostatic interactions<sup>[37,42]</sup>. The resultant powder was then collected via spray drying in a constant stirring, forming porous microspheres. The precursor underwent calcination at 700 °C in an inert atmosphere for 2 h, yielding flower-like porous nitrogen-doped MXene microspheres. Consequently, the synthesized 3D N-Ti<sub>3</sub>C<sub>2</sub>T<sub>x</sub> demonstrates remarkable thermal stability, which aligns with previous reports that the tailoring or functionalization of Ti<sub>3</sub>C<sub>2</sub> MXenes through polymers proficiently improves its stability<sup>[43,44]</sup>. As a comparative experiment, 3D Ti<sub>3</sub>C<sub>2</sub>T<sub>x</sub> microspheres were obtained by directly spray drying a pure Ti<sub>3</sub>C<sub>2</sub>T<sub>x</sub> solution, followed by calcination under identical conditions.

FESEM effectively captured the intricate morphology and microstructure. The precursor of Ti<sub>3</sub>AlC<sub>2</sub> (MAX phase) presents an inherent structure characterized by a dense stratification, as illustrated in [Supplementary Figure 2A](#). After HF etching, accordion-like MXenes can be obtained [[Supplementary Figure 2B](#)]. Then, few-layered MXenes can be synthesized by solution-phase flocculation strategy [[Supplementary Figure 2C](#)]<sup>[40]</sup>. In [Supplementary Figure 2D](#) and [E](#), 3D Ti<sub>3</sub>C<sub>2</sub>T<sub>x</sub> maintains the lamellar morphology of MXenes, with its surface exhibiting nanoparticles, presumably attributable to the

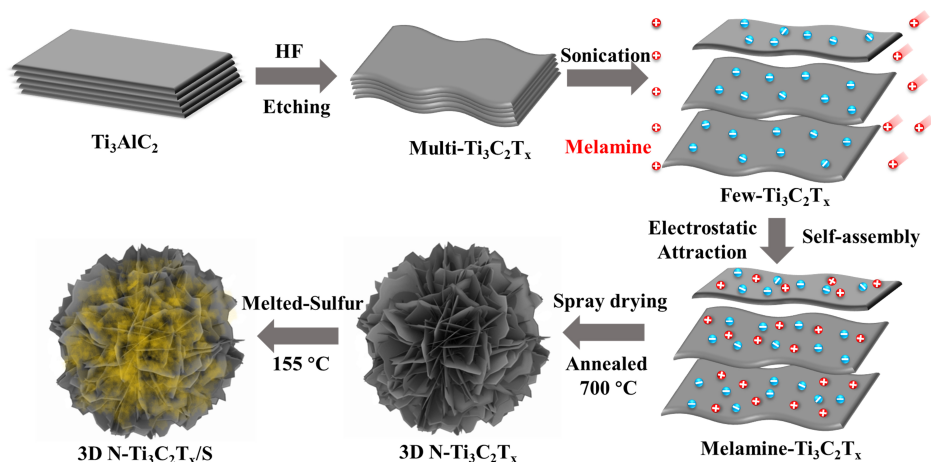


**Figure 1.** Schematic illustration of the synthesis process of 3D N-Ti<sub>3</sub>C<sub>2</sub>T<sub>x</sub> and 3D N-Ti<sub>3</sub>C<sub>2</sub>T<sub>x</sub>/S.

formation of TiO<sub>2</sub><sup>[45]</sup>. **Figure 2A** illustrates the morphology of the HCl-treated melamine/Ti<sub>3</sub>C<sub>2</sub>T<sub>x</sub> precursor. After spray drying, porous microspheres ranging from 2 to 10 μm formed. The 3D N-Ti<sub>3</sub>C<sub>2</sub>T<sub>x</sub> exhibits a nano-flower-shaped morphology composed of MXene nanosheets after annealing at 700 °C [**Figure 2B**]. As can be seen in **Supplementary Figure 2F**, the surface of these Ti<sub>3</sub>C<sub>2</sub>T<sub>x</sub> nanosheets is flat and smooth, with no observable TiO<sub>2</sub> nanoparticles. This intriguing observation suggests that the positively charged HCl-treated melamine coated itself on the surface of Ti<sub>3</sub>C<sub>2</sub>T<sub>x</sub> nanosheet layers through electrostatic self-assembly interaction, serving as a physical barrier to oxygen, effectively shielding the MXenes from oxidation during high-temperature processes. Consequently, the synthesized 3D N-Ti<sub>3</sub>C<sub>2</sub>T<sub>x</sub> demonstrates exceptional thermal stability.

The morphology and microstructure were further investigated via TEM. As shown in **Figure 2C-F**, TEM images provide a clearer view of 3D N-Ti<sub>3</sub>C<sub>2</sub>T<sub>x</sub>. Microspheres composed of MXene nanosheets can be observed. The lattice spacing corresponding to the MXenes (002) plane is approximately 1.5 nm [**Figure 2E**]. It is apparent that MXene nanosheets in 3D N-Ti<sub>3</sub>C<sub>2</sub>T<sub>x</sub> feature nano-sized micropores and mesopores at higher magnification, which could be attributed to the decomposition of melamine. These pores introduce defects, exposing more active sites to constrain LiPSs. Furthermore, C, Ti, and N elements are uniformly distributed within 3D N-Ti<sub>3</sub>C<sub>2</sub>T<sub>x</sub>, indicating the successful nitrogen doping into Ti<sub>3</sub>C<sub>2</sub>T<sub>x</sub> introduced by melamine decomposition [**Figure 2G**].

However, as shown in **Supplementary Figure 3**, the TiO<sub>2</sub> nanoparticle can be observed in TEM images, which demonstrates that Ti<sub>3</sub>C<sub>2</sub>T<sub>x</sub> undergoes substantial oxidation during thermal processing. As for 3D N-Ti<sub>3</sub>C<sub>2</sub>T<sub>x</sub>, melamine serves as a physical barrier to oxygen, effectively shielding the MXenes from oxidation.

After sulfur infusion, it is evident from the TEM and STEM images [**Supplementary Figure 4**] that sulfur has permeated uniformly into the layers of MXenes. Furthermore, the 3D N-Ti<sub>3</sub>C<sub>2</sub>T<sub>x</sub> has maintained its original nano-flower spherical architecture, exhibiting remarkable structural stability.

In order to demonstrate the electrostatic self-assembly interaction between HCl-melamine and few-layers Ti<sub>3</sub>C<sub>2</sub>T<sub>x</sub>, we tested the zeta potential of both [**Figure 3A**], and the results showed that they were positively charged and negatively charged, respectively, which was the origin of electrostatic self-assembly interaction.

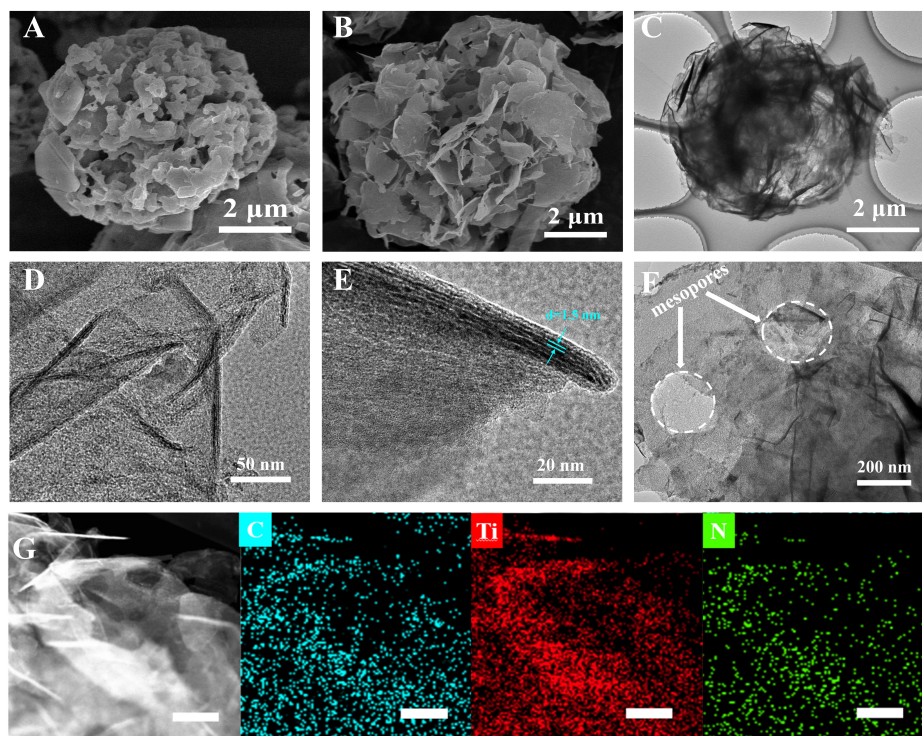


**Figure 2.** SEM images of (A) HCl-treated melamine/ $\text{Ti}_3\text{C}_2\text{T}_x$  precursor and (B) 3D N- $\text{Ti}_3\text{C}_2\text{T}_x$ , (C-F) TEM, and (G) STEM images of 3D N- $\text{Ti}_3\text{C}_2\text{T}_x$  with corresponding elemental mappings of C, Ti, and N. Scale bars: 200 nm.

XRD techniques investigated the structure of the synthesized 3D N- $\text{Ti}_3\text{C}_2\text{T}_x$ . As shown in [Figure 3B](#), compared to multilayered  $\text{Ti}_3\text{C}_2\text{T}_x$  MXenes, the low-angle diffraction peak for few-layered MXenes shifted from  $8.74^\circ$  to  $6.22^\circ$ , indicative of an increased interlayer spacing of the  $\text{Ti}_3\text{C}_2\text{T}_x$  MXenes (002) crystal plane. Furthermore, the XRD spectrum of 3D N- $\text{Ti}_3\text{C}_2\text{T}_x$  exhibited a peak at  $5.98^\circ$  for the (002) crystal plane, a  $0.24^\circ$  low-angle shift relative to few-layered  $\text{Ti}_3\text{C}_2$  MXenes ( $6.22^\circ$ ), which is attributed to nitrogen doping, as nitrogen atoms have a larger radius than carbon atoms, expanding interlayer spacing in MXenes<sup>[35]</sup>. [Figure 3C](#) illustrates the disappearance of the characteristic peak of the (104) crystal plane of  $\text{Ti}_3\text{AlC}_2$  in the XRD spectrum of multilayered  $\text{Ti}_3\text{C}_2$  MXenes, indicating the successful removal of aluminum atomic layers from  $\text{Ti}_3\text{AlC}_2$ . Without nitrogen doping, 3D  $\text{Ti}_3\text{C}_2\text{T}_x$  exhibited diffraction peaks at  $25.3^\circ$ , corresponding to the (101) crystal plane of anatase  $\text{TiO}_2$  (JCPDS#21-1272), consistent with the SEM and TEM images. This phenomenon indicates that oxidation occurs during the annealing, and on the contrary, the oxidation degree of 3D N- $\text{Ti}_3\text{C}_2\text{T}_x$  is low, indicating the protective effect of melamine on MXenes. The XRD pattern of 3D N- $\text{Ti}_3\text{C}_2\text{T}_x/\text{S}$  [[Supplementary Figure 5](#)] demonstrates the successful infusion of orthorhombic  $\text{S}_8$ .

Nitrogen adsorption-desorption tests under isothermal conditions on 3D N- $\text{Ti}_3\text{C}_2\text{T}_x$ , 3D  $\text{Ti}_3\text{C}_2\text{T}_x$ , 3D N- $\text{Ti}_3\text{C}_2\text{T}_x/\text{S}$ , and the melamine/MXenes precursor were conducted. The obtained isothermal adsorption-desorption curves were analyzed to further elucidate the pore structure and surface characteristics of the samples [[Figure 3D](#)]. The  $\text{N}_2$  adsorption-desorption curve for 3D N- $\text{Ti}_3\text{C}_2\text{T}_x$  exhibits a typical Type IV isotherm<sup>[46]</sup>, indicating the presence of abundant mesopores in the material, as observed from the pore size distribution image [[Figure 3E](#)]. The Brunauer-Emmett-Teller (BET) specific surface areas revealed that 3D N- $\text{Ti}_3\text{C}_2\text{T}_x$  possesses a substantial surface area of  $247.4 \text{ m}^2\text{g}^{-1}$  and a pore volume of  $0.83 \text{ cm}^3\text{g}^{-1}$ , while the melamine/MXenes precursor exhibited a specific surface area of  $22.2 \text{ m}^2\text{g}^{-1}$  and a pore volume of  $0.09 \text{ cm}^3\text{g}^{-1}$  [[Supplementary Figure 6A and B](#)]. These results highlight an increased porosity in 3D N- $\text{Ti}_3\text{C}_2\text{T}_x$  due to the

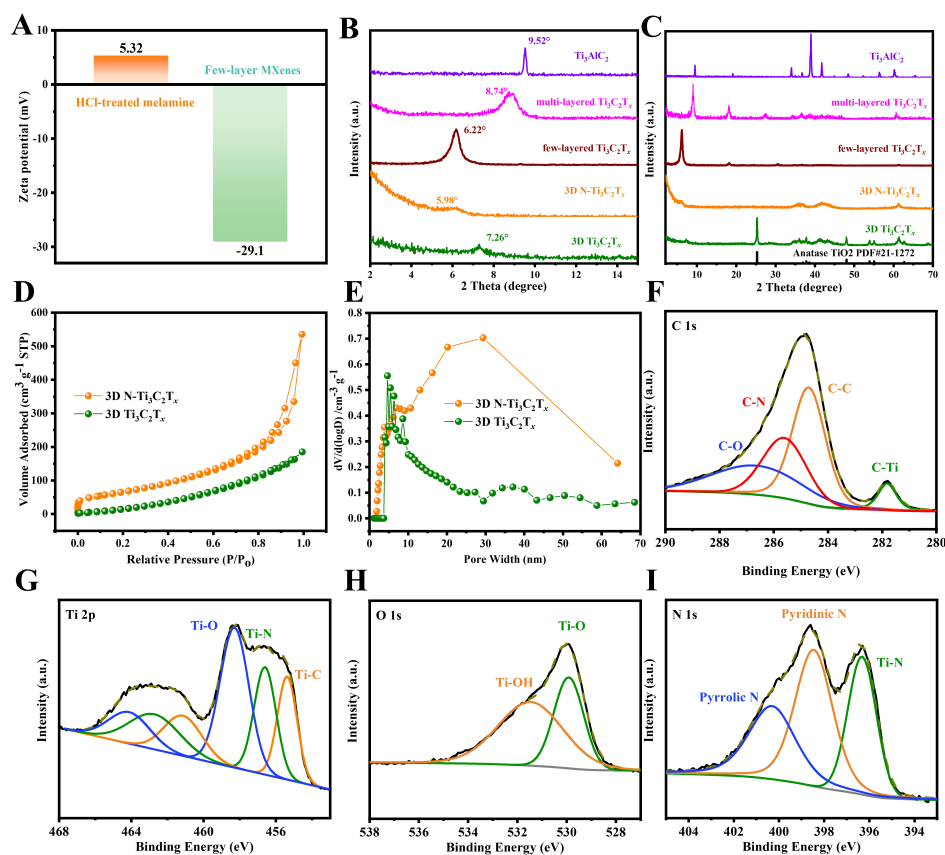


**Figure 3.** (A) The zeta potential of HCl-treated melamine and 3D N-Ti<sub>3</sub>C<sub>2</sub>T<sub>x</sub>. XRD patterns of Ti<sub>3</sub>AlC<sub>2</sub>, multi-layered Ti<sub>3</sub>C<sub>2</sub>T<sub>x</sub>, few-layered Ti<sub>3</sub>C<sub>2</sub>T<sub>x</sub> sheets and 3D N-Ti<sub>3</sub>C<sub>2</sub>T<sub>x</sub> with (B) 2θ from 2° to 15°, (C) 2θ from 2° to 70°. (D) N<sub>2</sub> adsorption-desorption isotherms and (E) pore-size distribution curves of 3D N-Ti<sub>3</sub>C<sub>2</sub>T<sub>x</sub> and 3D Ti<sub>3</sub>C<sub>2</sub>T<sub>x</sub>. XPS pattern of 3D N-Ti<sub>3</sub>C<sub>2</sub>T<sub>x</sub> (F) C 1s, (G) Ti 2p, (H) O 1s and (I) N 1s.

melamine decomposition during annealing, which will facilitate the adsorption of LiPSs and the maintenance of discharge capacity<sup>[47]</sup>. The porous structure not only facilitates uniform sulfur loading in 3D N-Ti<sub>3</sub>C<sub>2</sub>T<sub>x</sub> but also enhances electrolyte penetration and shortens ion/electron transport pathways. The specific surface area and pore volume of 3D N-Ti<sub>3</sub>C<sub>2</sub>T<sub>x</sub>/S significantly decrease compared to 3D N-Ti<sub>3</sub>C<sub>2</sub>T<sub>x</sub>, only 89.7 m<sup>2</sup>g<sup>-1</sup> and 0.22 cm<sup>3</sup>g<sup>-1</sup>, respectively [Supplementary Figure 6C and D]. This indicates that sulfur has embedded itself into the pores after sulfur infusion. For comparison, 3D Ti<sub>3</sub>C<sub>2</sub>T<sub>x</sub> displayed a lower specific surface area of 128.5 m<sup>2</sup>g<sup>-1</sup> and a pore volume of 0.28 cm<sup>3</sup>g<sup>-1</sup>.

The thermal gravimetric analysis (TGA) curves of the HCl-treated melamine/MXenes revealed a sharp weight drop at the temperature range of 250–350 °C [Supplementary Figure 7], which can be attributed to the melamine decomposition<sup>[41]</sup>. During annealing, active functional groups on the Ti<sub>3</sub>C<sub>2</sub>T<sub>x</sub> nanosheet surface, such as -F, -O, and -OH, are removed [Supplementary Figure 7], providing active sites suitable for nitrogen atom doping. The defects were introduced in the vicinity of doped nitrogen atoms<sup>[34]</sup>. Nitrogen-doped Ti<sub>3</sub>C<sub>2</sub>T<sub>x</sub> nanosheets exhibit significantly improved surface activities, resulting in a hydrophilic surface and enhanced Lewis acid absorption capability<sup>[48]</sup>.

Further analysis of the chemical composition and interactions was performed using XPS spectra. XPS spectra [Supplementary Figure 8A] of 3D Ti<sub>3</sub>C<sub>2</sub>T<sub>x</sub> and 3D N-Ti<sub>3</sub>C<sub>2</sub>T<sub>x</sub> both reveal the presence of C, O, and Ti elements, with the appearance of O elemental peaks attributed to surface-terminated functional groups

(-O, -OH) on  $\text{Ti}_3\text{C}_2\text{T}_x$ . **Figure 3F** and **Supplementary Figure 8B** compare the C 1s spectra of 3D  $\text{Ti}_3\text{C}_2\text{T}_x$  and 3D N- $\text{Ti}_3\text{C}_2\text{T}_x$ . The peaks at 281.8, 286.3, and 284.8 eV correspond to the C-Ti, C-O, and C-C bonds, respectively<sup>[32]</sup>. Furthermore, 3D N- $\text{Ti}_3\text{C}_2\text{T}_x$  exhibits an additional peak at 285.7 eV corresponding to the C-N bond<sup>[30]</sup>, and a noticeable decrease in peak intensity at 281.8 eV, possibly attributed to the removal of partial C-Ti bonds during nitrogen doping. In Ti 2p spectra, all two samples exhibit peaks associated with Ti-C bonds at 455.4 and 461.3 eV<sup>[49]</sup> and Ti-O bonds at 458.4 and 464.2 eV<sup>[50]</sup> [**Figure 3G** and **Supplementary Figure 8C**]. The Ti 2p spectrum of 3D N- $\text{Ti}_3\text{C}_2\text{T}_x$  shows two additional peaks at 456.6 and 462.9 eV, corresponding to Ti-N bonds<sup>[49]</sup>. The O 1s high-resolution XPS spectra of 3D  $\text{Ti}_3\text{C}_2\text{T}_x$  and 3D N- $\text{Ti}_3\text{C}_2\text{T}_x$  [**Figure 3H** and **Supplementary Figure 8D**] can be divided into characteristic peaks at 529.9 eV for Ti-O bonds and 531.5 eV for Ti-OH bonds<sup>[51]</sup>, corresponding to common surface-terminated functional groups (-O and -OH) on the MXene surface. The strong Ti-O bond signals indicate the formation of  $\text{TiO}_2$  in 3D  $\text{Ti}_3\text{C}_2\text{T}_x$ .

Besides, nitrogen elemental peaks are observed in 3D N- $\text{Ti}_3\text{C}_2\text{T}_x$ , indicating effective nitrogen doping. High-resolution N 1s XPS spectra of 3D N- $\text{Ti}_3\text{C}_2\text{T}_x$  [**Figure 3I**] reveal the chemical bonding properties of nitrogen. Peaks at 398.5 and 400.3 eV correspond to pyridinic and pyrrolic nitrogen, while a peak at 396.3 eV corresponds to Ti-N, further confirming the successful incorporation of nitrogen into MXene nanosheets<sup>[49]</sup>. Nitrogen, especially pyrrolic and pyridinic nitrogen in carbon lattice, enhances the affinity and chemical binding energy between the polar Ti atoms and sulfur and polar lithium polysulfides.

To validate the adsorption efficiency of 3D N- $\text{Ti}_3\text{C}_2\text{T}_x$  microspheres for LiPSs, visual adsorption experiment was applied to compare the adsorption capability of 3D N- $\text{Ti}_3\text{C}_2\text{T}_x$  and 3D  $\text{Ti}_3\text{C}_2\text{T}_x$  to LiPSs. **Figure 4A** shows the color fading of  $\text{Li}_2\text{S}_6$  solution with 3D N- $\text{Ti}_3\text{C}_2\text{T}_x$  and 3D  $\text{Ti}_3\text{C}_2\text{T}_x$ , respectively. The  $\text{Li}_2\text{S}_6$  solution containing 3D N- $\text{Ti}_3\text{C}_2\text{T}_x$  nearly faded completely, whereas the  $\text{Li}_2\text{S}_6$  solution containing 3D  $\text{Ti}_3\text{C}_2\text{T}_x$  remains yellow. This conclusion was further confirmed by corresponding UV-Vis spectroscopy, which showed an intensity decrease of the  $\text{Li}_2\text{S}_6$  solution peak within 3D N- $\text{Ti}_3\text{C}_2\text{T}_x$  compared to the others. Therefore, it can be concluded that 3D N- $\text{Ti}_3\text{C}_2\text{T}_x$  microspheres possess strong adsorption capabilities for LiPSs. This can be attributed to the enhanced polarity due to nitrogen doping and the higher specific surface area of 3D N- $\text{Ti}_3\text{C}_2\text{T}_x$ , which provides more adsorption sites for LiPSs. XPS analyses were applied to understand the chemical interaction between LiPSs and 3D N- $\text{Ti}_3\text{C}_2\text{T}_x$ . In the N 1s spectrum, the peaks shift to a higher binding energy after the adsorption of  $\text{Li}_2\text{S}_6$ , indicating the interaction between N and S atoms [**Figure 4B**]<sup>[52]</sup>. Besides, the proportion of configuration nitrogen had changed after the adsorption of  $\text{Li}_2\text{S}_6$ , as seen in **Supplementary Table 1**. Hence, it can be inferred that the pyridinic N and Ti-N are vital in the adsorption of  $\text{Li}_2\text{S}_6$ , because their relative proportions showed a greater decline<sup>[53]</sup>. In terms of the S 2p spectrum [**Figure 4C**], it can be divided into S-O, S-S and S-Ti bonds. Notably, the strong peak located at 169.8 eV can be attributed to S-O bonds, indicating the robust chemical binding ability of 3D N- $\text{Ti}_3\text{C}_2\text{T}_x$  to LiPSs<sup>[54]</sup>.

Symmetric cells with electrolytes containing  $\text{Li}_2\text{S}_6$  were assembled to evaluate the kinetics of LiPS conversion. The CV curves at 0.2  $\text{mV s}^{-1}$  [**Figure 4D**] revealed that 3D N- $\text{Ti}_3\text{C}_2\text{T}_x$  exhibited higher current response, more positive reduction peak potential, and more negative oxidation peak potential, indicating a larger surface area and nitrogen doping, providing additional polysulfide adsorption sites and faster kinetics for  $\text{Li}_2\text{S}_6$  redox conversion. Both 3D N- $\text{Ti}_3\text{C}_2\text{T}_x$  and 3D  $\text{Ti}_3\text{C}_2\text{T}_x$  electrodes displayed distinct oxidation-reduction peaks in CV curves at various scan rates (10~50  $\text{mV s}^{-1}$ ) [**Figure 4E** and **Supplementary Figure 9A**]. With increasing scan rate, the positions of the oxidation-reduction peaks slightly shifted, with the 3D N- $\text{Ti}_3\text{C}_2\text{T}_x$  electrode exhibiting narrower peak separations, suggesting stronger catalytic activity in polysulfide conversion.

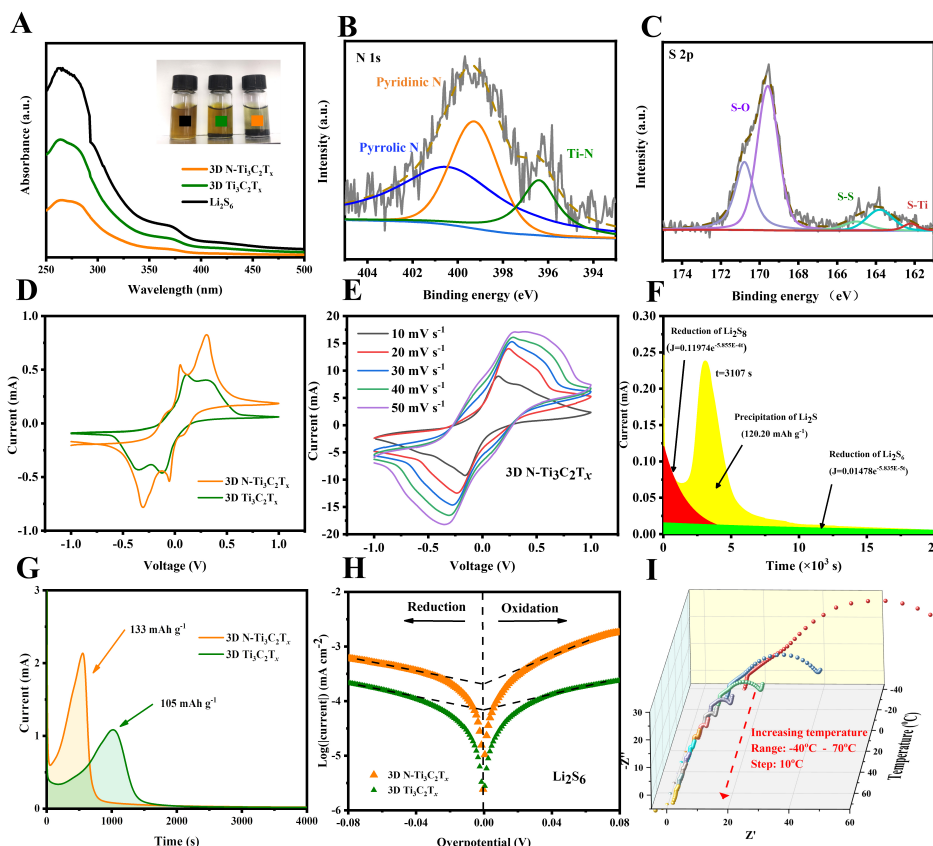


**Figure 4.** (A) UV-vis absorption spectra of the supernatant of  $\text{Li}_2\text{S}_6$  solution with 3D  $\text{Ti}_3\text{C}_2\text{T}_x$  and 3D  $\text{N-Ti}_3\text{C}_2\text{T}_x$  and the inset is a digital photograph. XPS pattern: (B) N 1s and (C) S 2p of 3D  $\text{N-Ti}_3\text{C}_2\text{T}_x$  after adsorption of  $\text{Li}_2\text{S}_6$ . The CV curves of symmetric cells with electrolytes containing  $\text{Li}_2\text{S}_6$ , (D) scan rate:  $0.2 \text{ mV s}^{-1}$  and (E) scan rate: 10 to  $50 \text{ mV s}^{-1}$  (3D  $\text{N-Ti}_3\text{C}_2\text{T}_x$ ). (F) The potentiostatic discharging profiles of  $\text{Li}_2\text{S}$  precipitation (at 2.05 V) for 3D  $\text{N-Ti}_3\text{C}_2\text{T}_x$ . (G) The potentiostatic discharging profiles of  $\text{Li}_2\text{S}$  dissolution (at 2.35 V) for 3D  $\text{N-Ti}_3\text{C}_2\text{T}_x$  and 3D  $\text{Ti}_3\text{C}_2\text{T}_x$ . (H) Tafel plot. (I) The EIS plot of 3D  $\text{N-Ti}_3\text{C}_2\text{T}_x$  symmetrical battery containing  $\text{Li}_2\text{S}_6$  electrolytes at different temperatures.

A potentiostatic  $\text{Li}_2\text{S}$  precipitation experiment was conducted to evaluate the catalytic effect of 3D  $\text{N-Ti}_3\text{C}_2\text{T}_x$  and 3D  $\text{Ti}_3\text{C}_2\text{T}_x$  on LiPS conversion. The results in Figure 4F and Supplementary Figure 9B show that 3D  $\text{N-Ti}_3\text{C}_2\text{T}_x$  displayed a higher peak current, earlier current response, and higher  $\text{Li}_2\text{S}$  precipitation capacity ( $120.20 \text{ mAh g}^{-1}$ ) than 3D  $\text{Ti}_3\text{C}_2\text{T}_x$ . These findings indicate the high catalytic activity of 3D  $\text{N-Ti}_3\text{C}_2\text{T}_x$  for  $\text{Li}_2\text{S}$  precipitation. Besides, we further investigated the impact of 3D  $\text{N-Ti}_3\text{C}_2\text{T}_x$  on the dissolution capacity of  $\text{Li}_2\text{S}$  during the charging process. As depicted in Figure 4G, 3D  $\text{N-Ti}_3\text{C}_2\text{T}_x$  exhibits a quicker current response and contributes significantly to the dissolution of  $\text{Li}_2\text{S}$ , which can be attributed to the superior electrical conductivity.

The enhanced redox kinetics from 3D  $\text{N-Ti}_3\text{C}_2\text{T}_x$  were further validated by exchanging current density [Figure 4H]. According to the fitting results of the Tafel plot, it exhibited a high exchange current density of  $3.16 \times 10^{-4} \text{ mA cm}^{-2}$ , remarkably larger than that of 3D  $\text{Ti}_3\text{C}_2\text{T}_x$  ( $1 \times 10^{-4} \text{ mA cm}^{-2}$ ), indicating a significant enhancement in redox kinetics.

In order to assess the performance of 3D  $\text{N-Ti}_3\text{C}_2\text{T}_x$  at both extremely high and low temperatures, we assembled a symmetrical battery containing  $\text{Li}_2\text{S}_6$  electrolytes and conducted EIS analysis at a temperature range from  $-40$  to  $70^\circ\text{C}$ . As shown in Figure 4I, the battery displays its highest internal resistance ( $R_i$ ) and

charge transfer resistance ( $R_{ct}$ ) at the frigid temperature of  $-40\text{ }^{\circ}\text{C}$ , primarily due to the slow  $\text{Li}^+$  transportation. As the temperature increases, the impedance progressively decreases, with the  $R_{ct}$  plummeting to a mere  $0.13\ \Omega$  at  $70\text{ }^{\circ}\text{C}$ , signaling 3D  $\text{N-Ti}_3\text{C}_2\text{T}_x$  facilitating charge transfer to LiPSs at high temperatures. Furthermore, an Arrhenius plot was constructed based on the  $R_{ct}$  values of the cell at varying temperatures [Supplementary Figure 9C], unveiling a notably linear correlation. The activation energy of the  $R_{ct}$  between 3D  $\text{N-Ti}_3\text{C}_2\text{T}_x$  and LiPSs was  $0.396\ \text{eV}$ .

The CR2032 coin cells with 3D  $\text{N-Ti}_3\text{C}_2\text{T}_x/\text{S}$  and 3D  $\text{Ti}_3\text{C}_2\text{T}_x/\text{S}$  cathodes were assembled to evaluate their electrochemical performance. TGA was also conducted on 3D  $\text{N-Ti}_3\text{C}_2\text{T}_x/\text{S}$ , 3D  $\text{Ti}_3\text{C}_2\text{T}_x/\text{S}$ , and pure sulfur to measure the sulfur content in the composites. As shown in Figure 5A, it is evident that all three samples exhibit significant mass loss at the temperature range of  $200\text{--}350\text{ }^{\circ}\text{C}$ , corresponding to the sublimation of sulfur under a nitrogen atmosphere. Accordingly, the sulfur content in 3D  $\text{N-Ti}_3\text{C}_2\text{T}_x/\text{S}$  and 3D  $\text{Ti}_3\text{C}_2\text{T}_x/\text{S}$  composites is measured as 72 and 66.4 wt%, respectively. CV tests were conducted in the voltage range of  $1.8\text{--}2.8\ \text{V}$  at a scan rate of  $0.1\ \text{mV s}^{-1}$  [Figure 5B]. Two cathodic peaks ( $2.28$  and  $2.05\ \text{V}$ ) correspond to the reduction of  $\text{S}_8$  to high-order LiPSs ( $\text{Li}_2\text{S}_x$ ,  $4 \leq x \leq 8$ ) and then to  $\text{Li}_2\text{S}_2/\text{Li}_2\text{S}$ , which has been described previously<sup>[55]</sup>. The positive cathodic peaks of the 3D  $\text{N-Ti}_3\text{C}_2\text{T}_x/\text{S}$  electrode indicate the effective catalytic activity to the LiPS conversion. Besides, as evidenced by the larger peak currents, the 3D  $\text{N-Ti}_3\text{C}_2\text{T}_x/\text{S}$  electrode exhibits superior redox kinetics to LiPSs. To further assess the impact on the LiPS conversion redox kinetics and lithium-ion diffusion, CV measurements at progressively increasing scan rates ranging from  $0.1$  to  $0.5\ \text{mV s}^{-1}$  were conducted [Figure 5C and Supplementary Figure 10A]. As the scan rate increased, the cathodic peaks shifted towards negative potentials, indicating a growing polarization. A similar phenomenon can be observed at anodic peaks. The diffusion coefficient of lithium ions ( $D_{\text{Li}^+}$ ) can be determined by calculating the slope of the current peaks against the square root of the scan rate, as given in the Randles-Sevcik equation<sup>[56]</sup>:  $I_p = (2.69 \times 10^5)n^{1.5}AD_{\text{Li}^+}^{0.5}C_{\text{Li}^+}\nu^{0.5}$ , where  $D_{\text{Li}^+}$  represents the lithium-ion diffusion coefficient, which can be derived from the peak current ( $I_p$ ).  $n$  is associated with the number of electrons transferred,  $A$  represents the electrode area,  $\nu$  denotes the sweeping rate, and  $C_{\text{Li}^+}$  signifies the concentration of lithium ions. Notably, the cell with a 3D  $\text{N-Ti}_3\text{C}_2\text{T}_x/\text{S}$  cathode demonstrated the steepest slopes in both the reduction and oxidation processes [Figure 5D and E and Supplementary Figure 10B]. This observation clearly indicates that the  $D_{\text{Li}^+}$  values of 3D  $\text{N-Ti}_3\text{C}_2\text{T}_x/\text{S}$  cathodes are significantly greater than those of 3D  $\text{Ti}_3\text{C}_2\text{T}_x/\text{S}$  cathodes.

To investigate the internal resistances of Li-S batteries with 3D  $\text{N-Ti}_3\text{C}_2\text{T}_x/\text{S}$  cathodes during the charging and discharging, the galvanostatic intermittent titration technique (GITT) was employed [Figure 5F]. The internal resistance associated with  $\text{Li}_2\text{S}$  nucleation and  $\text{Li}_2\text{S}$  activation was discernible through the depth of the dips observed in the charging and discharging profiles. Notably, the cell with a 3D  $\text{N-Ti}_3\text{C}_2\text{T}_x/\text{S}$  cathode shows a low discharge/charge polarization voltage plateau. The low potential variation between the points of  $\text{Li}_2\text{S}$  nucleation and  $\text{Li}_2\text{S}$  activation suggests the reduced polarization and enhanced kinetic efficiency.

Figure 6A presents the cycling performance of 3D  $\text{N-Ti}_3\text{C}_2\text{T}_x/\text{S}$  and 3D  $\text{Ti}_3\text{C}_2\text{T}_x/\text{S}$  electrodes at  $0.2\ \text{C}$ . The 3D  $\text{N-Ti}_3\text{C}_2\text{T}_x/\text{S}$  electrode exhibits an initial discharge capacity of  $1,115\ \text{mAh g}^{-1}$ , maintained at  $812.1\ \text{mAh g}^{-1}$  even after 150 cycles, significantly higher than that of the 3D  $\text{Ti}_3\text{C}_2\text{T}_x/\text{S}$ . The long-term cycling performance at  $0.5$  and  $1\ \text{C}$  is illustrated in Figure 6B and C, respectively. The 3D  $\text{N-Ti}_3\text{C}_2\text{T}_x/\text{S}$  electrode delivered a high initial capacity of  $937.0$  and  $853.7\ \text{mAh g}^{-1}$ , and maintained  $578.5\ \text{mAh g}^{-1}$  (500 cycles) and  $462.5\ \text{mAh g}^{-1}$  (1,000 cycles) at  $0.5$  and  $1\ \text{C}$ , corresponding to a low decay rate of  $0.076\%$  and  $0.046\%$  per cycle, respectively. Both are much better than that of 3D  $\text{Ti}_3\text{C}_2\text{T}_x/\text{S}$  electrodes. The 3D  $\text{N-Ti}_3\text{C}_2\text{T}_x/\text{S}$  electrode outperformed the 3D  $\text{Ti}_3\text{C}_2\text{T}_x/\text{S}$  electrode in terms of reversible capacity and cycling stability. These results collectively demonstrate that nitrogen doping improves the adsorption and sulfur conversion capabilities of 3D  $\text{N-Ti}_3\text{C}_2\text{T}_x$ , significantly enhancing the capacity and cycling stability of Li-S batteries.

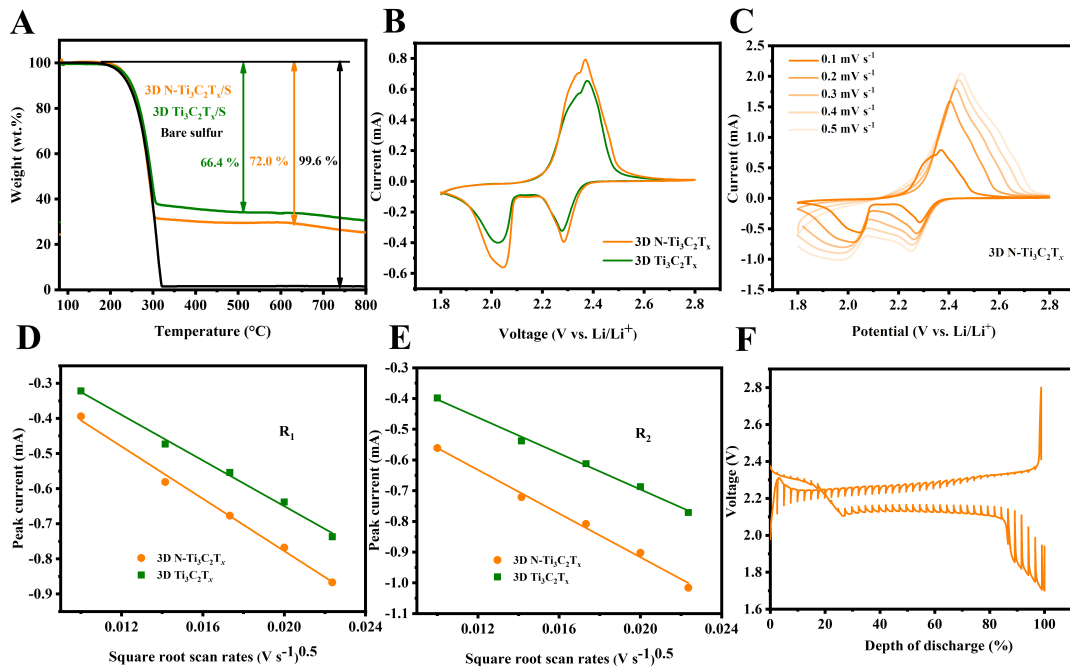


**Figure 5.** (A) TGA curves in Ar atmosphere. (B) 3D N-Ti<sub>3</sub>C<sub>2</sub>T<sub>x</sub>/S and 3D Ti<sub>3</sub>C<sub>2</sub>T<sub>x</sub>/S cathodes at the scanning rate of 0.1 mV s<sup>-1</sup>. (C) The CV curves of 3D N-Ti<sub>3</sub>C<sub>2</sub>T<sub>x</sub>/S cathodes at different scan rates. The plot of CV peak of (D) R<sub>1</sub> (S<sub>8</sub>-Li<sub>2</sub>S<sub>4</sub>) and (E) R<sub>2</sub> (Li<sub>2</sub>S<sub>4</sub>-Li<sub>2</sub>S) versus the square root of scan rates. (F) The GITT plot of the cell with 3D N-Ti<sub>3</sub>C<sub>2</sub>T<sub>x</sub>/S.

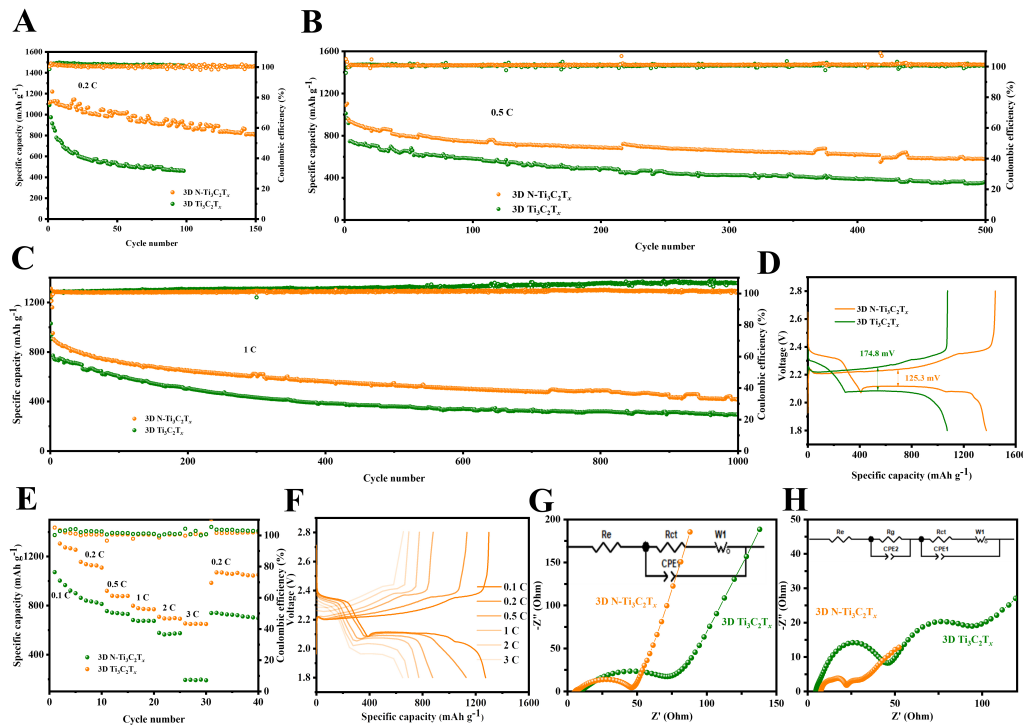


**Figure 6.** Cycle performance of 3D Ti<sub>3</sub>C<sub>2</sub>T<sub>x</sub>/S and 3D N-Ti<sub>3</sub>C<sub>2</sub>T<sub>x</sub>/S cathodes at (A) 0.2 C, (B) 0.5 C, and (C) 1 C. (D) The galvanostatic charge-discharge (GCD) profiles based on 3D N-Ti<sub>3</sub>C<sub>2</sub>T<sub>x</sub>/S and 3D Ti<sub>3</sub>C<sub>2</sub>T<sub>x</sub>/S cathode at 0.1 C. (E) Rate performance of 3D Ti<sub>3</sub>C<sub>2</sub>T<sub>x</sub>/S and 3D N-Ti<sub>3</sub>C<sub>2</sub>T<sub>x</sub>/S cathodes. (F) The GCD profiles of 3D N-Ti<sub>3</sub>C<sub>2</sub>T<sub>x</sub>/S at 0.1, 0.2, 0.5, 1, 2, and 3 C. Nyquist plots of 3D N-Ti<sub>3</sub>C<sub>2</sub>T<sub>x</sub>/S and 3D Ti<sub>3</sub>C<sub>2</sub>T<sub>x</sub>/S cathodes (G) before and (H) after cycles.

At 0.1 C, the battery demonstrates a distinctive charging plateau and two discharging plateaus [Figure 6D]. The charging plateau corresponds to the transformation of  $\text{Li}_2\text{S}_2/\text{Li}_2\text{S}$  into  $\text{S}_8$ . At the discharge process, the higher potential plateau is linked to the conversion of  $\text{S}_8$  into soluble high-order LiPSs, while the lower plateau is associated with the reduction of soluble LiPSs to  $\text{Li}_2\text{S}_2/\text{Li}_2\text{S}$ , which is consistent with the discussion of CV curves. Due to enhanced affinity of 3D N- $\text{Ti}_3\text{C}_2\text{T}_x$  to LiPSs and its catalytic performance, the kinetics of LiPS transformation have been markedly improved. Consequently, the polarization voltage ( $\Delta E$ ) measures 125.3 mV, noteworthy smaller than that of 3D  $\text{Ti}_3\text{C}_2\text{T}_x$ .

The rate performance tests were conducted at current densities ranging from 0.1 to 3 C [Figure 6E]. The 3D N- $\text{Ti}_3\text{C}_2\text{T}_x/\text{S}$  electrode achieved capacities of 1,274.1, 1,128.9, 876.8, 772.5, 694.3, and 651.2  $\text{mAh g}^{-1}$  at 0.1, 0.2, 0.5, 1, 2, and 3 C, respectively. When the current density is back to 0.2 C, the discharge capacity of 1,070.6  $\text{mAh g}^{-1}$  was achieved. In contrast, the 3D  $\text{Ti}_3\text{C}_2\text{T}_x/\text{S}$  electrode shows lower discharge specific capacities of 966.9, 833.5, 738.6, 675.8, 568.2, and 192.1  $\text{mAh g}^{-1}$  at the same rates, which means lower utilization of active material at high-rate conditions.

Figure 6F and Supplementary Figure 11 depict the GCD curves of the 3D N- $\text{Ti}_3\text{C}_2\text{T}_x/\text{S}$  and 3D  $\text{Ti}_3\text{C}_2\text{T}_x/\text{S}$  electrodes at different rates, respectively. The 3D N- $\text{Ti}_3\text{C}_2\text{T}_x/\text{S}$  electrode displayed two typical discharge plateaus, corresponding to the conversion of  $\text{S}_8$  to long-chain LiPSs and the subsequent conversion to  $\text{Li}_2\text{S}_2/\text{Li}_2\text{S}$ , respectively. All discharge curves of 3D N- $\text{Ti}_3\text{C}_2\text{T}_x/\text{S}$  exhibited two characteristic plateaus even at a high current of 3 C. However, the discharge curves of 3D  $\text{Ti}_3\text{C}_2\text{T}_x/\text{S}$  show vague plateaus, indicating lower sulfur utilization than 3D N- $\text{Ti}_3\text{C}_2\text{T}_x/\text{S}$ .

EIS tests further validated the improvement in electrochemical performance before and after 100 cycles at 0.5 C [Figure 6G and H]. Compared to the 3D  $\text{Ti}_3\text{C}_2\text{T}_x/\text{S}$  electrode, the pristine EIS curve of the 3D N- $\text{Ti}_3\text{C}_2\text{T}_x/\text{S}$  electrode exhibits a smaller semicircle shape in the high-frequency region, indicating that nitrogen doping enhances the conductivity of  $\text{Ti}_3\text{C}_2\text{T}_x$  MXenes. After 100 cycles, the  $R_{ct}$  of the 3D N- $\text{Ti}_3\text{C}_2\text{T}_x/\text{S}$  electrode is significantly lower than that of 3D  $\text{Ti}_3\text{C}_2\text{T}_x/\text{S}$ , which is attributed to the large surface area of 3D N- $\text{Ti}_3\text{C}_2\text{T}_x$  for electrolyte infiltration and lithium-ion transport. Additionally, nitrogen doping promotes the formation and conversion of  $\text{Li}_2\text{S}$ . This further underscores that the porous structure of 3D N- $\text{Ti}_3\text{C}_2\text{T}_x$  can provide ample diffusion pathways, and nitrogen doping can effectively immobilize polysulfides, reducing irreversible consumption of sulfur and lithium passivation caused by shuttle effects, enabling the battery to maintain high electron/ion transfer rates, thereby enhancing the electrochemical performance. To explore the potential for practical application, the cells with high sulfur loadings (2.4 and 4.2  $\text{mg cm}^{-2}$ ) were assembled. As depicted in Supplementary Figure 12, the cell with 2.4  $\text{mg cm}^{-2}$  sulfur loading exhibits an areal capacity close to 1.8  $\text{mAh cm}^{-2}$  at 2 C, and the cell with 4.2  $\text{mg cm}^{-2}$  sulfur loading can maintain a capacity of 3  $\text{mAh cm}^{-2}$  at 1 C, experiencing a capacity reduction only at 2 C. This observation underscores the electrochemical performance of 3D N- $\text{Ti}_3\text{C}_2\text{T}_x/\text{S}$  with a high sulfur loading.

The deterioration of lithium anodes is related to the severe shuttle effects<sup>[57]</sup>. Additionally, the degree of polysulfide dissolution can be evaluated by the simple optical photograph of the separators after cycling. Supplementary Figure 13A depicts the scanning images of the disassembled lithium anode. It can be observed that the lithium anode surface is exceptionally smooth before cycling. After cycling, the lithium anode surface with 3D  $\text{Ti}_3\text{C}_2\text{T}_x/\text{S}$  exhibits pulverization and cracks, along with a significant accumulation of dead lithium [Supplementary Figure 13B], while the battery with 3D N- $\text{Ti}_3\text{C}_2\text{T}_x/\text{S}$  is relatively smoother, and only a small amount of lithium dendrites can be observed [Supplementary Figure 13C]. As shown in

[Supplementary Figure 13D](#), the separator of the 3D  $\text{Ti}_3\text{C}_2\text{T}_x/\text{S}$  cell (left) is covered with a thick layer of dark yellow substance, corresponding to the LiPSs. However, only a small amount of yellow precipitate remains on the separator with the 3D N- $\text{Ti}_3\text{C}_2\text{T}_x/\text{S}$  cathode (right). All the above results show that 3D N- $\text{Ti}_3\text{C}_2\text{T}_x$  can effectively alleviate the shuttle effect in Li-S batteries, and excellent electrochemical performance can be achieved.

## CONCLUSIONS

In summary, few-layered  $\text{Ti}_3\text{C}_2\text{T}_x$  was obtained, and 3D N- $\text{Ti}_3\text{C}_2\text{T}_x$  was successfully synthesized by spray drying. Positively charged HCl-melamine is electrostatically attached to the surface of negatively charged MXenes, preventing the aggregation of MXene nanosheets and enhancing its thermal stability. Spray drying facilitates the transformation of unique nanoflower-shaped microspheres, endowing 3D N- $\text{Ti}_3\text{C}_2\text{T}_x$  with a large specific surface area and pore volume. Due to the synergistic effect of the large specific surface area and nitrogen doping, MXenes exhibit increased adsorption capacity and catalytic conversion ability for LiPSs, effectively preventing the shuttle effect. Therefore, high-capacity retention (578.5 mAh  $\text{g}^{-1}$  after 500 cycles at 0.5 C, and 462.5 mAh  $\text{g}^{-1}$  after 1,000 cycles at 1 C remained), superior rate performance (651.2 mAh  $\text{g}^{-1}$  at 3 C), and excellent long-term cycling performance (capacity fading rate of 0.076% per cycle at 0.5 C and 0.046% per cycle at 1 C) have been achieved. This work broadens the application of MXenes and provides new insight into the practical use of Li-S batteries.

## DECLARATIONS

### Authors' contributions

Formal analysis, investigation, writing - original draft: Cai L, Ying H

Formal analysis, writing - review: He C

Formal analysis, investigation, writing - review: Tan H

Gave advice and methodology to the research: Huang P, Han Q

Supervision, investigation, resources, writing - review and editing: Han WQ

### Availability of data and materials

More data on our findings can be found in the [Supplementary Material](#).

### Financial support and sponsorship

This work is supported by the Natural Science Foundation of Zhejiang Province (No. LY23E020008), the Key Research and Development Program of Zhejiang Province (No. 2023C01127), the Technologies R&D Program of Huzhou City (No. 2022JB01), "Dongjiang Talent Program" of Qidong City, Highstar Corporation HSD20210118.

### Conflicts of interest

All authors declared that there are no conflicts of interest.

### Ethical approval and consent to participate

Not applicable.

### Consent for publication

Not applicable.

### Copyright

© The Author(s) 2024.

## REFERENCES

1. Wang J, Han W. A review of heteroatom doped materials for advanced lithium-sulfur batteries. *Adv Funct Mater* 2022;32:2107166. DOI
2. Feng J, Li J, Zhang H, et al. Accelerating redox kinetics by ZIF-67 derived amorphous cobalt phosphide electrocatalyst for high-performance lithium-sulfur batteries. *Energy Mater* 2023;3:300001. DOI
3. Tan H, Wang J, Huang P, et al. Facile synthesis of high-content nitrogen-doped hierarchical porous carbon spheres for high-capacity lithium-sulfur batteries. *J Mater Sci* 2023;58:2700-12. DOI
4. Guo R, Zhang S, Wang J, Ying H, Han W. One-pot synthesis of a copolymer micelle crosslinked binder with multiple lithium-ion diffusion pathways for lithium-sulfur batteries. *ChemSusChem* 2020;13:819-26. DOI
5. Meng Z, Zhang S, Wang J, et al. Nickel-based-hydroxide-wrapped activated carbon cloth/sulfur composite with tree-bark-like structure for high-performance freestanding sulfur cathode. *ACS Appl Energy Mater* 2018;1:1594-602. DOI
6. Cui X, Wang X, Pan Q. Achieving fast and stable  $\text{Li}^+$  transport in lithium-sulfur battery via a high ionic conduction and high adhesion solid polymer electrolyte. *Energy Mater* 2023;3:300034. DOI
7. Xian C, Wang Q, Xia Y, et al. Solid-state electrolytes in lithium-sulfur batteries: latest progresses and prospects. *Small* 2023;19:e2208164. DOI
8. Raza H, Bai S, Cheng J, et al. Li-S batteries: challenges, achievements and opportunities. *Electrochem Energy Rev* 2023;6:29. DOI
9. Meng Z, Li S, Ying H, Xu X, Zhu X, Han W. From silica sphere to hollow carbon nitride-based sphere: rational design of sulfur host with both chemisorption and physical confinement. *Adv Mater Inter* 2017;4:1601195. DOI
10. Ruan J, Sun H, Song Y, et al. Constructing 1D/2D interwoven carbonous matrix to enable high-efficiency sulfur immobilization in Li-S battery. *Energy Mater* 2022;1:100018. DOI
11. Chen P, Wang T, He D, et al. Delocalized isoelectronic heterostructured  $\text{FeCoO}_x\text{S}_y$  catalysts with tunable electron density for accelerated sulfur redox kinetics in Li-S batteries. *Angew Chem Int Ed* 2023;62:e202311693. DOI
12. Xu H, Hu R, Zhang Y, et al. Nano high-entropy alloy with strong affinity driving fast polysulfide conversion towards stable lithium sulfur batteries. *Energy Storage Mater* 2021;43:212-20. DOI
13. Zhou Z, Chen Z, Lv H, et al. High-entropy nanoparticle constructed porous honeycomb as a 3D sulfur host for lithium polysulfide adsorption and catalytic conversion in Li-S batteries. *J Mater Chem A* 2023;11:5883-94. DOI
14. Zeng P, Zhou X, Peng J, et al. Promoting "strong adsorption" and "fast conversion" of polysulfides in Li-S batteries based on conductive sulfides host with hollow prism structure and surface defects. *Adv Funct Mater* 2023;33:2211818. DOI
15. Chen X, Zhao C, Yang K, et al. Conducting polymers meet lithium-sulfur batteries: progress, challenges, and perspectives. *Energy Environ Mater* 2023;6:e12483. DOI
16. Naguib M, Kurtoglu M, Presser V, et al. Two-dimensional nanocrystals produced by exfoliation of  $\text{Ti}_3\text{AlC}_2$ . *Adv Mater* 2011;23:4248-53. DOI
17. Chu X, Wang Y, Cai L, et al. Boosting the energy density of aqueous MXene-based supercapacitor by integrating 3D conducting polymer hydrogel cathode. *SusMat* 2022;2:379-90. DOI
18. Liu R, Zhai S, Ye Z, et al. Constructing carbon nanotube-optimized hollow  $\text{Ti}_3\text{C}_2$  MXene hierarchical conductive networks for robust lithium-sulfur batteries. *J Mater Chem A* 2023;11:24330-7. DOI
19. Zhang X, Ni Z, Bai X, et al. Hierarchical porous n-doped carbon encapsulated fluorine-free MXene with tunable coordination chemistry by one-pot etching strategy for lithium-sulfur batteries. *Adv Energy Mater* 2023;13:2301349. DOI
20. Wang X, Guo J, Xu K, et al. In situ self-assembled  $\text{NiS}_2$  nanoparticles on MXene nanosheets as multifunctional separators: regulating shuttling effect and boosting redox reaction kinetics of lithium polysulfides. *Appl Surface Sci* 2024;645:158859. DOI
21. Zhang D, Wang S, Hu R, et al. Catalytic conversion of polysulfides on single atom zinc implanted mxene toward high-rate lithium-sulfur batteries. *Adv Funct Mater* 2020;30:2002471. DOI
22. Liao L, Wang S, Duan H, Deng Y. MXene-based materials: synthesis, structure and their application for advanced lithium-sulfur batteries. *J Energy Storage* 2024;75:109555. DOI
23. Xu S, Zhang Y, Shi Y, Qian Q, Wang C, Qiu J. Enhancing the cycling stability of Li-S batteries with flexible freestanding sulfur cathodes through a spider-hunting strategy. *Chem Eng J* 2024;479:147869. DOI
24. Xiang M, Shen Z, Zheng J, et al. Gas-phase synthesis of  $\text{Ti}_2\text{CCl}_2$  enables an efficient catalyst for lithium-sulfur batteries. *Innovation* 2024;5:100540. DOI PubMed PMC
25. Huang Z, Jaumaux P, Sun B, et al. High-energy room-temperature sodium-sulfur and sodium-selenium batteries for sustainable energy storage. *Electrochem Energy Rev* 2023;6:21. DOI
26. Liu A, Liang X, Ren X, Guan W, Ma T. Recent progress in MXene-based materials for metal-sulfur and metal-air batteries: potential high-performance electrodes. *Electrochem Energy Rev* 2022;5:112-44. DOI
27. Bashir T, Zhou S, Yang S, et al. Progress in 3D-MXene electrodes for lithium/sodium/potassium/magnesium/zinc/aluminum-ion batteries. *Electrochem Energy Rev* 2023;6:5. DOI
28. Zhao MQ, Sedran M, Ling Z, et al. Synthesis of carbon/sulfur nanolaminates by electrochemical extraction of titanium from  $\text{Ti}_2\text{SC}$ . *Angew Chem Int Ed* 2015;54:4810-4. DOI
29. Liang X, Garsuch A, Nazar LF. Sulfur cathodes based on conductive MXene nanosheets for high-performance lithium-sulfur batteries. *Angew Chem Int Ed* 2015;54:3907-11. DOI PubMed
30. Huang P, Ying H, Zhang S, Zhang Z, Han W. Multidimensional synergistic architecture of  $\text{Ti}_3\text{C}_2$  MXene/ $\text{CoS}_2$ @N-doped carbon for

- sodium-ion batteries with ultralong cycle lifespan. *Chem Eng J* 2022;429:132396. DOI
31. Huang P, Zhang S, Ying H, Zhang Z, Han W. Few-layered  $Ti_3C_2$  MXene anchoring bimetallic selenide  $NiCo_2Se_4$  nanoparticles for superior Sodium-ion batteries. *Chem Eng J* 2021;417:129161. DOI
  32. Zhang S, Ying H, Huang P, et al. Rational design of pillared  $SnS/Ti_3C_2T_x$  MXene for superior lithium-ion storage. *ACS Nano* 2020;14:17665-74. DOI
  33. Yang C, Tang Y, Tian Y, et al. Flexible nitrogen-doped 2D titanium carbides (MXene) films constructed by an ex situ solvothermal method with extraordinary volumetric capacitance. *Adv Energy Mater* 2018;8:1802087. DOI
  34. Bao W, Liu L, Wang C, Choi S, Wang D, Wang G. Facile synthesis of crumpled nitrogen-doped MXene nanosheets as a new sulfur host for lithium-sulfur batteries. *Adv Energy Mater* 2018;8:1702485. DOI
  35. Wen Y, Rufford TE, Chen X, et al. Nitrogen-doped  $Ti_3C_2T_x$  MXene electrodes for high-performance supercapacitors. *Nano Energy* 2017;38:368-76. DOI
  36. Zhang S, Ying H, Guo R, Yang W, Han WQ. Vapor deposition red phosphorus to prepare nitrogen-doped  $Ti_3C_2T_x$  MXenes composites for lithium-ion batteries. *J Phys Chem Lett* 2019;10:6446-54. DOI
  37. Yoon Y, Lee M, Kim SK, et al. A strategy for synthesis of carbon nitride induced chemically doped 2D MXene for high-performance supercapacitor electrodes. *Adv Energy Mater* 2018;8:1703173. DOI
  38. Jiang G, Zheng N, Chen X, et al. In-situ decoration of MOF-derived carbon on nitrogen-doped ultrathin MXene nanosheets to multifunctionalize separators for stable Li-S batteries. *Chem Eng J* 2019;373:1309-18. DOI
  39. Song Y, Sun Z, Fan Z, et al. Rational design of porous nitrogen-doped  $Ti_3C_2$  MXene as a multifunctional electrocatalyst for Li-S chemistry. *Nano Energy* 2020;70:104555. DOI
  40. Zhang S, Huang P, Wang J, Zhuang Z, Zhang Z, Han WQ. Fast and Universal Solution-Phase Flocculation Strategy for Scalable Synthesis of Various Few-Layered MXene Powders. *J Phys Chem Lett* 2020;11:1247-54. DOI
  41. Wang J, Yan X, Zhang Z, et al. Facile preparation of high-content N-doped CNT microspheres for high-performance lithium storage. *Adv Funct Mater* 2019;29:1904819. DOI
  42. Ye Z, Jiang Y, Li L, Wu F, Chen R. Self-assembly of 0D-2D heterostructure electrocatalyst from MOF and MXene for boosted lithium polysulfide conversion reaction. *Adv Mater* 2021;33:e2101204. DOI
  43. Wang G, Yang Z, Wu L, Wang J, Liu X. Studies on improved stability and electrochemical activity of titanium carbide MXene-polymer nanocomposites. *J Electroanal Chem* 2021;900:115708. DOI
  44. Carey M, Barsoum M. MXene polymer nanocomposites: a review. *Mater Today Adv* 2021;9:100120. DOI
  45. Zhang H, Song J, Li J, et al. Interlayer-expanded  $MoS_2$  nanoflowers vertically aligned on MXene@dual-phased  $TiO_2$  as high-performance anode for sodium-ion batteries. *ACS Appl Mater Interfaces* 2022;14:16300-9. DOI
  46. Chen Z, Xu Y, Zhao W, et al. Mesoporous silicas tethered with anions as quasi-solid electrolytes for lithium-metal batteries. *Chem Commun* 2022;58:13656-9. DOI
  47. Ruan J, Lei YJ, Fan Y, et al. Linearly Interlinked  $Fe-N_x-Fe$  single atoms catalyze high-rate sodium-sulfur batteries. *Adv Mater* 2024;36:2312207. DOI
  48. Wei C, Tian M, Fan Z, et al. Concurrent realization of dendrite-free anode and high-loading cathode via 3D printed N- $Ti_3C_2$  MXene framework toward advanced Li-S full batteries. *Energy Storage Mater* 2021;41:141-51. DOI
  49. Amiri A, Chen Y, Bee Teng C, Naraghi M. Porous nitrogen-doped MXene-based electrodes for capacitive deionization. *Energy Storage Mater* 2020;25:731-9. DOI
  50. Zhang S, Ying H, Huang P, Yang T, Han W. Hierarchical utilization of raw  $Ti_3C_2T_x$  MXene for fast preparation of various  $Ti_3C_2T_x$  MXene derivatives. *Nano Res* 2022;15:2746-55. DOI
  51. Huang P, Zhang S, Ying H, et al. Fabrication of Fe nanocomplex pillared few-layered  $Ti_3C_2T_x$  MXene with enhanced rate performance for lithium-ion batteries. *Nano Res* 2021;14:1218-27. DOI
  52. Cai J, Sun Z, Cai W, et al. A robust ternary heterostructured electrocatalyst with conformal graphene chainmail for expediting bi-directional sulfur redox in Li-S batteries. *Adv Funct Mater* 2021;31:2100586. DOI
  53. Zhang M, Lu C, Bi Z, et al. Preparation of highly pyrrolic-nitrogen-doped carbon aerogels for lithium-sulfur batteries. *ChemElectroChem* 2021;8:895-902. DOI
  54. Ma C, Jia X, Liu X, et al. Ultrafine NbN nanoparticle decorated nitrogen-doped carbon nanosheets with efficient polysulfide catalytic conversion for superior Li-S batteries. *J Power Sources* 2022;520:230764. DOI
  55. Cai L, Ying H, Huang P, et al. In-situ grown  $Ti_3C_2T_x@CoSe_2$  heterostructure as trapping-electrocatalyst for accelerating polysulfides conversion in lithium-sulfur battery. *Chem Eng J* 2023;474:145862. DOI
  56. Zhou G, Tian H, Jin Y, et al. Catalytic oxidation of  $Li_2S$  on the surface of metal sulfides for Li-S batteries. *Proc Natl Acad Sci USA* 2017;114:840-5. DOI PubMed PMC
  57. Huang Y, Lin L, Zhang C, et al. Recent advances and strategies toward polysulfides shuttle inhibition for high-performance Li-S batteries. *Adv Sci* 2022;9:e2106004. DOI PubMed PMC